DTU Library

Electrochemical Reduction of CO2 on IrxRu(1−x)O2(110) Surfaces

Bhowmik, Arghya; Hansen, Heine Anton; Vegge, Tejs

Electrochemical reduction of CO_2 on $Ir_xRu_{(1-x)}O_2$ (110) surfaces

Arghya Bhowmik, Dr. Heine Anton Hansen* and Prof. Dr. Tejs Vegge

Department of Energy Conversion and Storage, Technical University of Denmark, Fysikvej Bldg. 309,

DK-2800 Kgs. Lyngby, Denmark.

E-mail: heih@dtu.dk; Fax: +45 46 77 57 58; Tel: +45 45 25 82 11

Table of Contents Graphic
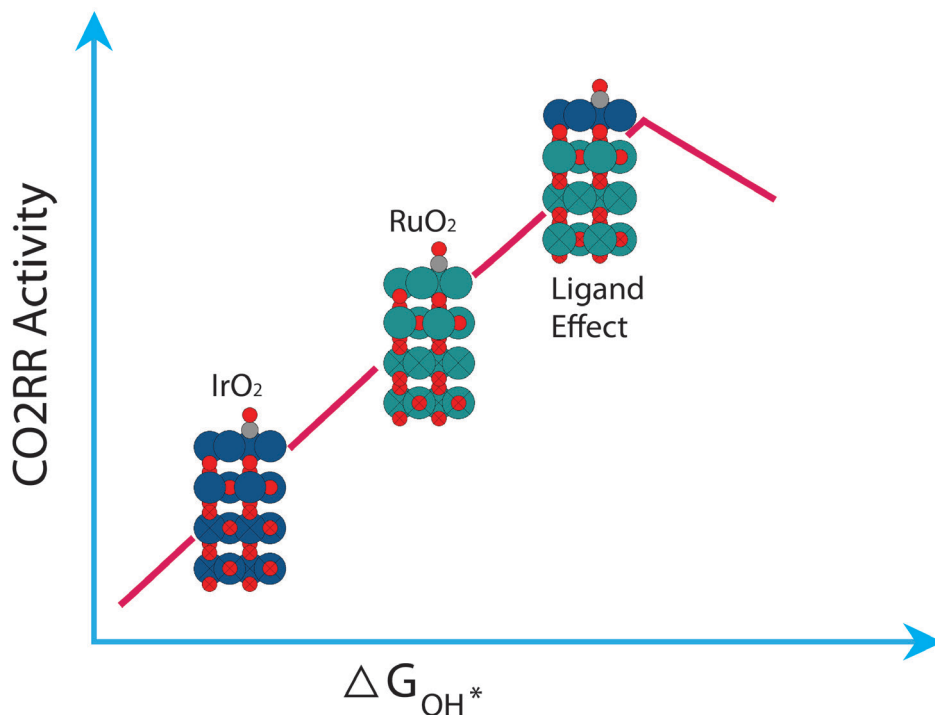
Abstract

High overpotentials and low faradic efficiencies plague metal catalysts for direct conversion of CO_2 to methanol and other liquid fuels. RuO_2 based electrocatalysts have been observed to evolve methanol at low overpotential, which has been attributed to an alternative reaction mechanism with oxygen coordinated intermediates that can circumvent the limitations imposed by the scaling relations on metal catalysts. Here, we introduce an innovative concept of ligand effects in oxide catalysts. Both IrO_2 and RuO_2

binds OH* and other CO2RR intermediates strongly, but the stable and miscible system $Ir_xRu_{(1-x)}O_2$ exhibits anomalous weaker binding energy in presence of CO* spectators due to Ru-Ir ligand effects. The weakened adsorbate binding leads to very low CO2RR onset potential (methanol evolution at -0.2 V-RHE). An Ir atom at the bridge site with Ru neighbors binds intermediates like OH* and OCHO* much weaker, due to synergistic ligand effects and adsorbate-adsorbate interactions. Consequently, a RuO_2 surface doped with Ir move close to the top of the predicted CO2RR volcano for oxides, which offers a significant improvement over state of the art electrocatalysts for conversion of CO_2 into methanol. Analysis of electronic structure parameters with adsorbate binding energies indicates the ligand effect depletes electrons from the Ir atom and shifts the t2g orbitals. The lack of electron donation from CO* spectators to Ir at the active site cause favorable adsorbate binding.

Subject keywords: Computational catalysis, Density Functional Theory, Electrochemical CO_2 reduction, Rutile oxide, Ligand Effect, Adsorbate Interaction

Introduction

As consensus builds regarding the role of anthropogenic CO_2 emission as a fundamental cause behind increasing weather anomalies and global warming, the need to develop new technologies to enable growth without the associated CO_2 emissions becomes ever clearer[1–3]. Mankind has already mastered the art of harnessing electrical energy from renewable sources like solar and wind in an inexpensive manner, but challenges remain within the fossil fuel dependent transport sector and in large-scale energy storage, which deters the transition to a carbon neutral society[2,4–6]. Electrochemical reduction of CO_2 (CO2RR) into fuels and chemicals using renewable electricity can prove to be a key technology as it can provide cheap long-term mobile energy storage while being carbon neutral. Efficient electrochemical conversion of CO_2 directly to energy carriers like methanol or ethanol is not yet feasible at high current densities due to the lack of electrocatalysts, which can activate such reaction at low overpotentials and high product selectivity by suppressing the parasitic hydrogen evolution reaction (HER). Most single metal catalysts produce either mostly hydrogen, CO or formic acid[7–9]; the exception being copper, which produces hydrocarbons at moderate Faradaic efficiency, but requires an overpotential of $\eta > 1.0$ V for a modest current density of 1 mA/cm^2, reducing the energy storage efficiency[10]. Density functional theory (DFT) based computational studies on the CO2RR pathway and thermodynamic barriers have been done previously for metal catalysts[11,12]. Such analyses have illustrated that on metal catalysts, the reduction of adsorbed CO (CO*) to formyl (CHO*) is the thermodynamically limiting step in the reduction of CO_2 to hydrocarbons. The linear scaling relation between the adsorption energies of the two critical reaction intermediates CO* and CHO* makes it difficult to improve the overpotential by choosing stronger or weaker binding single metal catalysts[11]. As the binding energy difference between CO* and CHO* stays similar for different metal surfaces, the potential required to reduce CO* to CHO* remain unchanged. Similarly, the reduction of CO_2 to CO on

metal catalysts go through COOH* intermediate whose binding energy is strongly correlated with CO*. Thus the most suitable binding energy combination of CO* and COOH* (leading to best activity) is not accessible together by choice of a different metal catalyst[12,13]. A class of sparingly studied rutile structured oxide materials has been observed to convert CO_2 into methanol at low overpotential[14–18]. Pourbaix diagrams suggest that IrO_2 and RuO_2 at neutral pH and reducing condition are eventually reduced to metals. However, X-ray photoelectron spectroscopy (XPS) studies show that RuO_2 maintains its oxidized state under reducing conditions[19]. This kinetic stability can be attributed to a large kinetic barrier for leaching subsurface oxygen out. In an electrochemical environment, IrO_2 shows even higher stability than RuO_2[20] and will remain as an oxide at reducing conditions.

Recent theoretical studies have established the different catalytic behaviors of such oxide catalysts compared to metal catalysts originate from differences in the CO2RR pathway[21,22]. The O-coordinated reaction intermediates dominate the pathway on oxide surfaces and obey different scaling relations,[21] thereby circumventing the limitations of the metal electrocatalysts. The OH* binding energy is proven to be a good (single) descriptor for such catalysts' activity, as it scales with the binding energy of other reaction intermediates in CO2RR. Engineering the OH* binding strength on oxide surfaces, therefore, provides a handle towards optimizing CO2RR catalyst performance[21].

Metal alloys often show intermediate adsorbate binding energies compared to the constituent metals. This gives rise to an interesting approach to catalyst design. Combining two metals: one with too strong adsorption (left leg of the activity volcano) and one with too weak adsorption (right leg of the volcano), one can create a catalyst surface with an optimum reaction intermediate binding energy to be at the top of the volcano curve. This interpolation principle has been successfully implemented to create new highly active catalysts for nitrogen reduction to ammonia[23] and CO_2 reduction to methanol[24]. Another approach for CO2RR electrocatalyst design is alloying with a metal with high oxygen affinity and interacts with some adsorbates through the oxygen atom. This would lead to a two-descriptor scenario, effectively breaking the CO*/CHO* binding scaling limitation[11].

A study of the OH* biding on mixed oxides can equip us to fine tune catalyst activity for CO2RR. $Ru_xIr_{(1-x)}O_2$ mixed oxide systems provides an excellent possibility to explore the adsorbate binding energy landscape. Lattice parameters for the rutile IrO_2 and RuO_2 oxides are well matched and for both oxides, the (110) surface has the lowest energy and is thus predominantly accessible for catalysis[25,26]. Based on the CO2RR reaction mechanism and analysis of the adsorbate binding energy scaling relations, the left leg of the CO2RR activity volcano on rutile oxide surfaces is limited by OH* removal[21]. RuO_2 falls on the left of the volcano. Thus, surfaces with OH* adsorption slightly weaker than RuO_2 (110) should have a lower overpotential. IrO_2 binds OH* stronger than RuO_2 [27]. However, an Ir-oxide overlayer on RuO_2 have weaker OH* binding energy than pure RuO_2; thereby apparently violating the interpolation principle. Hence, unlike some metal alloys, detailed simulations are necessary to predict the catalytic properties of mixed oxides.

Adsorbate binding energies are sensitive to strain as well as ligand effects originating from variations in the nature of elements in the vicinity of the adsorption site. Alloyed catalysts with large strain are prone to degradation, due to leaching and segregation; thus utilizing ligand effects for modulating the OH* binding energy in mixed oxides is a better strategy to maintain catalyst stability. $Ru_xIr_{1-x}O_2$ (110) surfaces are excellent model mixed oxide surfaces for studying catalytic properties. RuO_2 and IrO_2 have been widely researched as catalysts[18,25,28–43]. Both oxides are good band conductors[44] as required for electrocatalysis. IrO_2 and RuO_2 are both found in the rutile type crystals structure in pure form and lattice parameters match closely[45]. Especially for the (110) surface, the change in composition would not bring forth any lateral strain, which can affect the binding energy for adsorbates. The a lattice parameter (defining the in-plane strain in (110) plane) is less than 0.3% percent higher for IrO_2 than RuO_2. This is much lower than the 1-4% strain needed to have any significant modification in catalytic activity[46–49]. Thus, ligand effects will dominate variations in binding energies on $Ru_xIr_{1-x}O_2$ (110) surfaces.

The close match in crystal structure and unit cell parameters helps $Ru_xIr_{1-x}O_2$ mixed oxide system to be stable over long periods of time. This system is miscible for a wide range of composition[50]. Segregation can otherwise be a challenge for long lifetime of electrocatalyst as structural evolutions change the catalytic properties[51–56]. The bulk mixing energy as well as overlayer adhesion is exothermic[57] for $Ru_xIr_{1-x}O_2$ – supporting the excellent stability of the system. Indeed, the mixed oxide has been shown to be more stable than pure RuO_2 and suitable for long-term operation as an electrocatalyst[31].

Here, we systematically study the binding energy and reaction path on $Ru_xIr_{1-x}O_2$ catalyst surfaces to explore their suitability for CO2RR. $Ru_xIr_{1-x}O_2$ mixed oxide systems can be active at moderate over-potential if the trend observed for the Ir-oxide overlayer on RuO_2 holds for other mixed oxide structures[21]. While single metal atom doped oxide catalysts have been studied theoretically[58–61], a methodical study of the catalytic pathway under compositional variation in any mixed oxide system is absent. Our study also elucidates how key adsorbates like H*/OH*/CO* binds to mixed Ru-Ir-oxides with varying Ru-Ir characteristics.

Previous work[21,62] reveal that the CO* coverage can drastically modify the adsorbate binding, affecting both the CO2RR onset potential as well as selectivity over HER, where a small amount of spurious CO evolution can alter the CO* surface coverage. Consequently, CO* coverage effects on mixed oxide surfaces are also studied simultaneously for a wide range of Ir/Ru-mixed oxide surfaces. The CO* adsorption behavior is nonlinear as the composition changes from pure RuO_2 to pure IrO_2 and the adsorbate interaction has pronounced effects, explicitly for the intermediate composition range. Finally, a large reaction network for CO2RR consisting of 27 possible reaction intermediates with oxygen and carbon coordinated adsorbates and various products are explored on a range of $Ru_xIr_{1-x}O_2$(110) mixed oxide surfaces, to create an understanding of composition and CO* coverage effects for efficient CO2RR to liquid fuel conversion.

Computational method

The density functional theory (DFT) based simulation tool Vienna ab-initio simulation package (VASP)[63], is used here to simulate model catalyst surfaces with and without adsorbates. The BEEF-vdW[64] exchange correlation functional with the vdW-DF2[65] nonlocal correlation energy and potential is used here to properly represent adsorbate interactions[66,67]. Details of molecular and adsorbate free energy calculations are reported in the supporting information. To estimate the change in free energy under an applied potential for elementary proton transfer steps, the reaction thermodynamic are calculated using the computational hydrogen electrode (CHE) model[68].

A comprehensive DFT-based study of the CO2RR thermodynamic process is complex and computationally demanding due to the multiple reaction pathways possible. Modelling the mixed oxide system $Ru_xIr_{1-x}O_2$ can be further complicated by many conceivable cation distributions. To avoid such complexity of cation distribution, previous theoretical study involved either substitution of a single atom in a RuO_2 or IrO_2 bulk/surface; or replacement of all the top layer cations in the simulation slab, keeping the bottom layers fixed to the bulk lattice structure[57]. Such simplification of the mixed oxide system needs to be considered, especially if complete reaction pathway for CO2RR needs to be simulated on each model oxide surface.
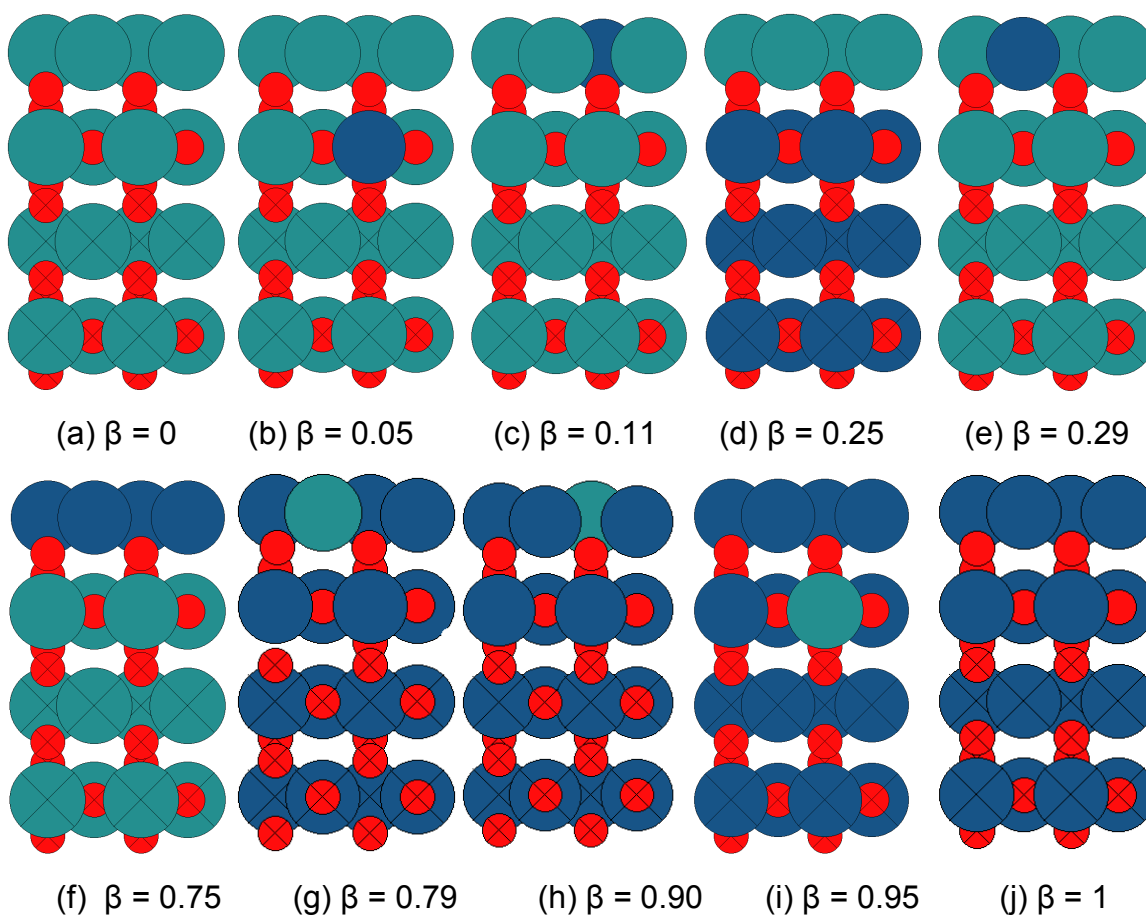
In the absence of strain, adsorption energy variation in mixed oxides with composition will come from the geometry of the active site and the chemical environment of the atoms surrounding it. Cation substitution closest to the active site would impact the binding energy more than a substitution in a different atomic layer further away. Thus, by single cation substitution at different positions relative to the active site, a range of mixed oxide catalytic behaviors can be represented.

To understand the differences emanating from the different configurations of Ir/Ru cation distributions near the active site, we consider 10 different model rutile (110) surfaces of these oxides starting from pure RuO_2 to pure IrO_2 surface (Figure 1). Surface slabs are prepared with four cation layers following previous theoretical work[21,22]. Bridging oxygen atoms were removed to model the reducing environment during the CO2RR. RuO_2 and IrO_2 surfaces are made based on the optimized bulk structure of the respective oxides and cations are substituted to make mixed oxides. Each surface is given an index, β, based on the Ru or Ir character of the bridge site. The procedure is detailed in supporting information section.

The bridge site has been identified as the active site for the CO2RR[21,22,62]. Comprehensive DFT based theoretical study has been done on the energetics of cation replacement in (110) surface of IrO_2 and RuO_2[57]. It indicates that replacement of Ru atoms in RuO2 with Ir atoms and Ir atoms in IrO2 with Ru atoms are favorable. Formation of full overlayer is stable for this oxides' (110) surfaces[57]. Single cation replacement can be done at one of the metal sites supporting the bridge site, at the coordinately unsaturated (cus) site in the top atom layer or below the bridge site in the 2nd atomic layer (Figure 1).

These model surfaces have two bridge sites and two cus sites in the repeating unit cell. In our simulations, we consider three possible CO* spectator configurations: (a) no CO*

spectator, (b) one CO* spectator at one bridge site, (c) two CO* spectators, one at bridge site and the other at the cus site next to it (Figure 1 (k-l)). This corresponds to 0%, 25% and 50% CO* coverage, respectively. The selection of these representative CO* coverage models was done based on our analysis of CO* coverage effects on CO2RR for RuO_2 catalyst[62]. We have studied the effects of CO* spectator coverage/ordering and found that oxygen coordinated reaction intermediates like OH* prefer (based on binding free energy calculations) to occupy bridge sites of the (110) surface rather than cus sites. The same preference is much less prominent for CO* adsorbate. Thus, a (110) surface with both the type of adsorbates would preferentially have OH* at the bridge site and CO* occupying other bridge and cus sites.
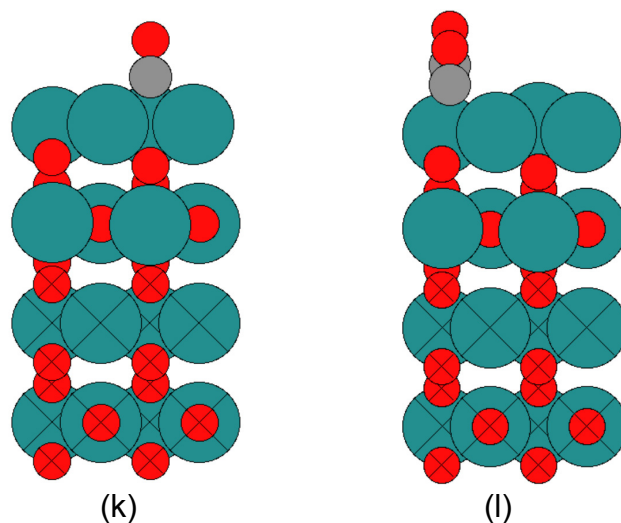

(a) β = 0   (b) β = 0.05   (c) β = 0.11   (d) β = 0.25   (e) β = 0.29

(f) β = 0.75   (g) β = 0.79   (h) β = 0.90   (i) β = 0.95   (j) β = 1

Figure 1: (a) Pure RuO_2 slab. (b) In a RuO_2 slab, one Ru atom replaced with Ir atom in the 2nd atomic layer below the bridge site. (c) In a RuO_2 slab, one Ru atom at the coordinately unsaturated (cus) site replaced with Ir. (d) In an IrO_2 slab, all Ir atoms in the top layer replaced with Ru. (e) In a RuO_2 slab, one Ru atom at the bridge site replaced with Ir (f) In a RuO_2 slab, all Ru atoms in the top layer replaced with Ir. (g) In an IrO_2 slab, one Ir atom at the bridge site replaced with Ru. (h) In an IrO_2 slab One Ir atom at the cus site replaced with Ru. (i) In an IrO_2 slab, one Ir atom replaced with a Ru atom in the 2nd atomic layer below the bridge site. (j) Pure IrO_2 slab. (k) RuO_2 slab with 25% CO* coverage (bridge site) (l) RuO_2 slab with 50% CO* (bridge and cus site). Green, blue and red spheres are Ru, Ir and O atoms, respectively. the β index is a measure of Ir character (between 0 and 1) of the bridge site based on the partial radial distribution of Ru and Ir atoms around the bridge site. All surfaces are (110).

Results and discussion

Composition and spectator effects on adsorbate binding

The adsorption free energies of H*, OH* (Figure 2) and CO* (Table 1) are calculated to understand how composition and spectators affect the binding energy of key reaction intermediates and subsequently the catalytic activity. Surfaces with high Ir-character bind H* much stronger than those with high Ru-character across different CO* spectator coverage. The surface binding H* the strongest is the IrO_2 surfaces with a single Ru atom at the cus site for 25% or 50% CO* coverage. Without any CO* coverage, an Ir-oxide overlayer on Ru-oxide shows the strongest H* binding. The presence of up to 50% CO* spectator coverage weakens the H* binding by 0.2 eV or less for surfaces rich in ruthenium. On the contrary, surfaces rich in Ir shows a slight increase in the H* binding strength.

Surfaces with mixed character, e.g. β=0.75 or β=0.29, show a strong repulsive adsorbate-adsorbate interaction and the H* binding decreases by up to 0.65 eV. Although weak binding H* leads to low overpotential for the HER, H* fails to bind to the

surface because strong binding OH* and other CO2RR intermediates have a thermodynamic preference, effectively blocking HER.

A similarly opposing adsorbate-adsorbate interaction effect is observed on intermediate index surfaces with β=0.29, 0.75, 0.79 for the OH*-CO* interaction. OH* is much stronger bonded to the surfaces with Ir atoms than Ru rich surfaces. The presence of CO* spectators makes OH* bind stronger than without CO* coverage on Ru or Ir rich surfaces (β = 0, 0.5, 0.11, 0.25 and β = 0.9, 0.95, 1.0). On the intermediate surfaces β=0.29, 0.75, 0.79, the CO* adsorbate interaction is repulsive for OH* binding and OH* is thus destabilized by up to 0.4 eV. Based on the thermodynamic volcano for CO2RR on oxide catalysts, this weakening of OH* binding should lead to equal amount of lower overpotential for CO2RR as OH* removal forms the left leg of the volcano[21].

The 1st CO* binding at the bare surface bridge site is favorable by 1 eV or more for all surfaces (Table1). The 1st CO* molecule is more stable on surfaces with β close to zero than those close to 1. This is opposite to the behavior observed for H* and OH* adsorbates. However, more striking is the exceptionally high stability of the 1st CO* adsorbate on surfaces with an active site with at least one coordinating Ir atom, which has Ru neighbors (β=0.29, 0.75, 0.79). For surfaces with mainly Ru character, the CO*-CO* adsorbate interaction is repulsive, it is strongly repulsive for intermediate compositions (0.25 < β < 0.8), but attractive for Ir-rich surfaces (β > 0.8). On surfaces with a single Ir atom close to the bridge site of a RuO_2 slab, such CO*-CO* interaction will limit the CO* coverage and provide sufficient active sites for CO2RR with favorable OH* binding associated. Vice-versa, Ir-rich surfaces (β=0.9, 0.95, 1.0) can accommodate high CO* coverage, due to the attractive CO*-CO* interaction and fail to activate CO_2.

Under reaction conditions, adsorbates like O* [69], H* [70] and CO* [71] have been shown to create preferential conditions for one metal to segregate at the surface over the other metal. Stronger adsorption of the species on one type of metal over another causes this segregation. Replacement of a ruthenium atom by an iridium atom in a bare RuO_2 (110) slab is most favorable at the subsurface layer. Replacement is less favorable at cus site (+0.11 eV w.r.t subsurface) or next to bridge site (+0.09 w.r.t subsurface). Replacement of one iridium atom by a ruthenium atom in a bare IrO_2 (110) slab, is most favorable at the bridge site and least favorable at the subsurface layer. The energy difference between these two configurations is even smaller at 0.06 eV. The thermodynamic driving force is very small for adsorbate induced surface segregation. Thus for large enough kinetic barriers (limiting diffusion), substitution will occur nearly randomly between these three sites. With H*, OH* and CO* adsorbates, some sites are better suited for cation substitution than others (Table 2). For the Ir doped RuO_2 (110) surface, Ir is preferred close to the bridge site in the presence of H*, OH*, or CO* adsorbates. For the Ru doped IrO_2 (110) slab, the Ru dopant is preferred at the cus site in presence of H*/OH* adsorbates, while the Ru dopant prefers the bridge site in the presence of CO*. CO* spectators can induce bridge site segregation at low cation doping in IrO_2/RuO_2 surfaces if the kinetic barriers are surmountable. This leads to bridge sites coordinated with one Ir and one Ru atom. Thus CO* spectator also enhances the ligand effects in catalyst properties.

Table 1: Variation of CO* binding free energy at the bridge site due to Ir/Ru mixed oxide composition and CO* spectators. Lightest share means highest value and darkest is the lowest value

β	0.00	0.05	0.11	0.25	0.29	0.75	0.79	0.90	0.95	1.00
CO* spectator coverage	CO* adsorption free energy at bridge site (eV)									
0%	-1.34	-1.23	-1.29	-1.15	-1.58	-1.62	-1.56	-1.17	-0.98	-1.10
25%	-0.90	-1.06	-0.84	-0.99	-0.72	-0.71	-0.53	-1.34	-1.42	-1.42
50%	-0.77	-0.9	-0.77	-0.83	-0.51	-0.64	-0.32	-1.26	-1.36	-1.33

Table 2: Adsorbate induced preference for cation substitution position

adsorbate	Energy difference of Ir atom substitution position in RuO_2 slab w.r.t. bridge site substitution			Energy difference of Ru atom substitution position in IrO_2 slab w.r.t. bridge site substitution		
	Bridge β=0.29	Cus β=0.11	Subsurface β=0.05	Bridge β=0.79	Cus β=0.9	Subsurface β=0.95
None	0.00	0.02	-0.09	0.00	0.06	0.00
H*	0.00	0.19	0.10	0.00	-0.07	-0.02
OH*	0.00	0.39	0.23	0.00	-0.23	0.04
CO*	0.00	0.32	0.27	0.00	0.45	0.19

We have previously established a thermodynamic volcano for CO2RR activity on RuO_2-based rutile oxide surfaces with the OH* binding energy as descriptor[21]. Here, OH* binding energies between -0.25 eV and 0.25 eV were found to be very favorable for CO2RR activity. The weakening of the OH* binding energy on partially CO* covered surfaces with mixed Ir-Ru characteristics compared to pure IrO_2 or RuO_2 surfaces moves the investigated mixed oxide surfaces closer to top of the activity volcano. Additionally, a weak H* binding on these partially CO* covered surfaces support selectivity by promoting OCHO* formation at the active site instead of H*. The fundamentally different behavior of adsorbate binding and strong CO* spectator interaction on surfaces where the bridge site has an Ir atom which in turn have Ru as cation neighbor is striking and the key to the suitable binding energy behavior.
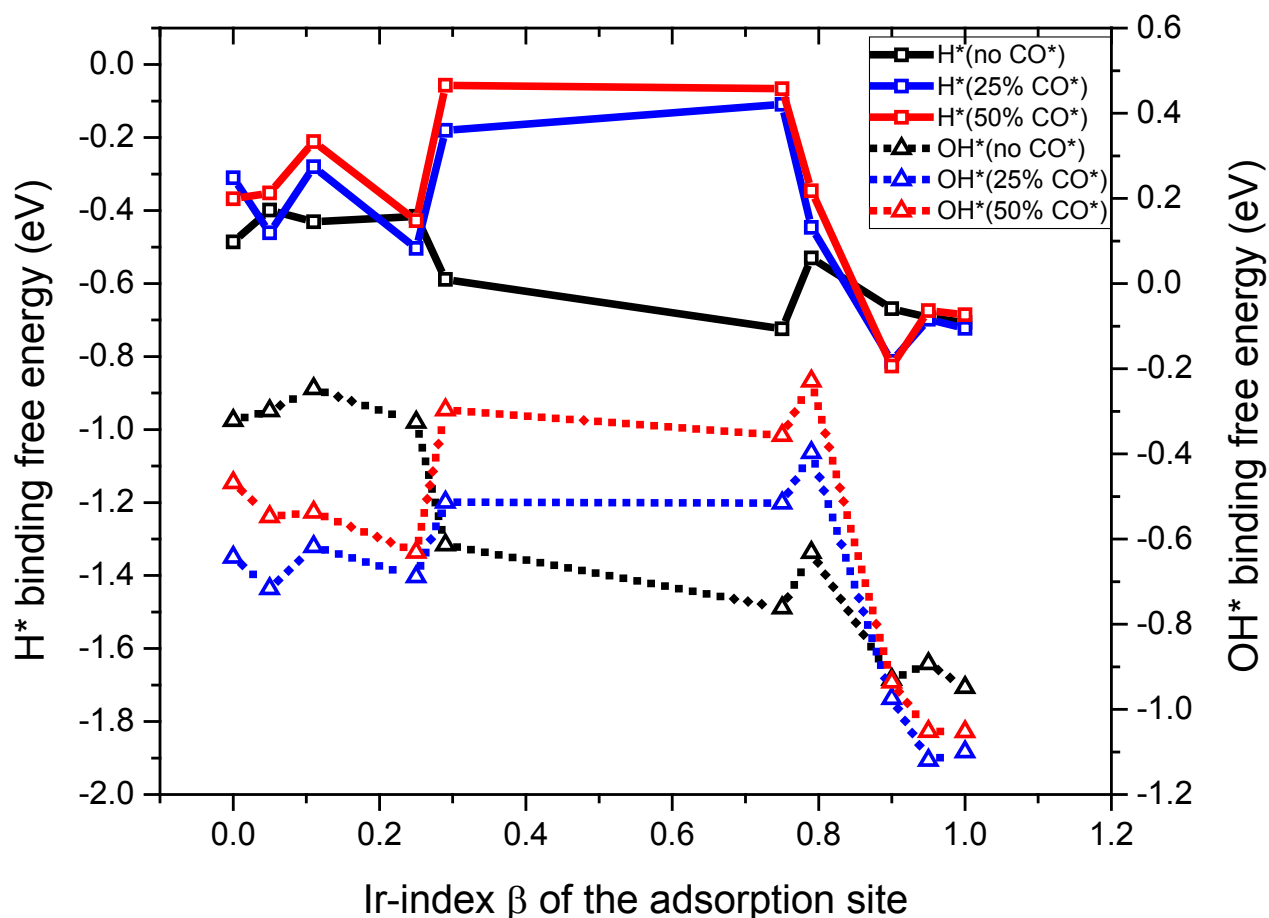
Figure 2: H*/OH* binding energy on Ru-Ir mixed oxide surfaces at varying CO* spectator coverage.

CO_2 activation

The first reaction step in CO2RR leads to formation of OCHO* or COOH* from protonation of CO_2. H* can form if CO_2 molecules are not available close to the reaction site or the CO_2 activation barrier is very high (>1 eV). Reported values for proton transfer to COOH* formation on Pt[72] (0.55 eV), OCHO* formation on Pb[73] (0.25 eV) suggest the CO_2 activation barrier to be small enough to be surmountable at room temperature. We assume the kinetic barriers are small and proportional to free energy change of the reactions step. Thus, reaction intermediates that are more stable are readily formed. On pure RuO_2 (110) and Ir-oxide overlayer on RuO_2(110), the stability order for the 1st electron transfer products is ΔG[OCHO] < ΔG[H] < ΔG[COOH][21]. This relative ordering of stability holds true for all surfaces studied here. Thus, with good availability of CO_2 molecules and protons in the electrolyte layer close to catalyst surface, CO2RR activity dominates over HER on this class of mixed oxides. OCHO* binds strongest on Ir-rich surfaces and Ru-rich surfaces with 25% CO* coverage (Table 3). Although COOH* is less stable than OCHO* in the absence of CO* spectators and on Ir-rich surfaces with any CO* coverage, the formation of COOH* is downhill in free energy at 0 V-RHE and thus side reactions can proceed through this intermediate.

Further protonation of COOH* forms H$_2$O and leaves another CO* adsorbate as products.

Thus a bare Ir-Ru mixed oxide surface would develop a ~25% CO* coverage over time under CO2RR conditions. Only on Ir-rich surfaces (β≥0.9) can COOH* intermediates form spontaneously at 0 V-RHE even with higher CO* coverage and increase the CO* coverage on further reduction. The relative stability of OCHO* intermediate with respect to COOH* intermediate is provided in Table S2. The thermodynamics of high CO* coverage on Ir-rich surfaces has been discussed in the previous section.

Table 3: Binding free energy of COOH* and OCHO* intermediates formed from CO$_2$ activation. Lightest share means highest value and darkest is the lowest value.

β	0.00	0.05	0.11	0.25	0.29	0.75	0.79	0.90	0.95	1.00
CO* spectator coverage	COOH* binding free energy (eV)									
0%	0.27	-0.17	-0.02	0.11	-0.35	-0.43	-0.34	-0.71	-0.58	-0.64
25%	0.08	0.02	0.13	0.05	0.41	0.11	0.13	-0.23	-0.39	-0.29
50%	0.31	0.23	0.29	0.13	0.71	0.21	0.29	-0.02	-0.21	-0.16

β	0.00	0.05	0.11	0.25	0.29	0.75	0.79	0.90	0.95	1.00
CO* spectator coverage	OCHO* binding free energy (eV)									
0%	-0.81	-0.81	-0.80	-0.89	-0.95	-1.10	-1.15	-1.33	-1.25	-1.28
25%	-1.04	-1.07	-1.00	-1.13	-0.71	-0.55	-0.65	-1.23	-1.27	-1.24
50%	-0.71	-0.75	-0.78	-0.88	-0.30	-0.29	-0.54	-1.03	-1.20	-1.16

CO2RR pathway

One of the main challenges in simulating CO2RR at the atomic scale is the complexity of the possible reaction network. Restricting the intermediates to those with a single carbon atom is a reasonable assumption, as the reported products from rutile oxide CO2RR catalysts are primarily C$_1$ type[14,16–18]. Our previous theoretical studies of CO2RR on oxide overlayers on RuO$_2$(110) surface did not include C-coordinated reaction intermediates like CHO*, COH*, C*, CH*, CH$_2$*, CH$_3$*, due to the higher stability of O-coordinated intermediates on RuO$_2$(110)[21,22]. Here, we have included such intermediates to confirm that O-coordinated intermediates are indeed preferred reaction intermediates as the surface composition is varied.

All the reaction intermediates (involving adsorbates and free molecules) simulated on the mixed oxide surfaces are listed in Table S1. This reaction network is sufficient to understand the reaction mechanism and onset potential limitations of formic acid, methanol and methane production. All intermediates are simulated with 3 different configurations of spectator CO* coverage. All adsorbates are bound to the bridge site and OCHO*/ H$_2$COOH* being bidentate (supplementary figure S1) also occupy a cus site along with the bridge site. The thermodynamic free energy diagrams for all surfaces

and CO* configurations with all 26 reaction intermediates are provided as supplementary information. The full reaction network considered is depicted in figure 3.
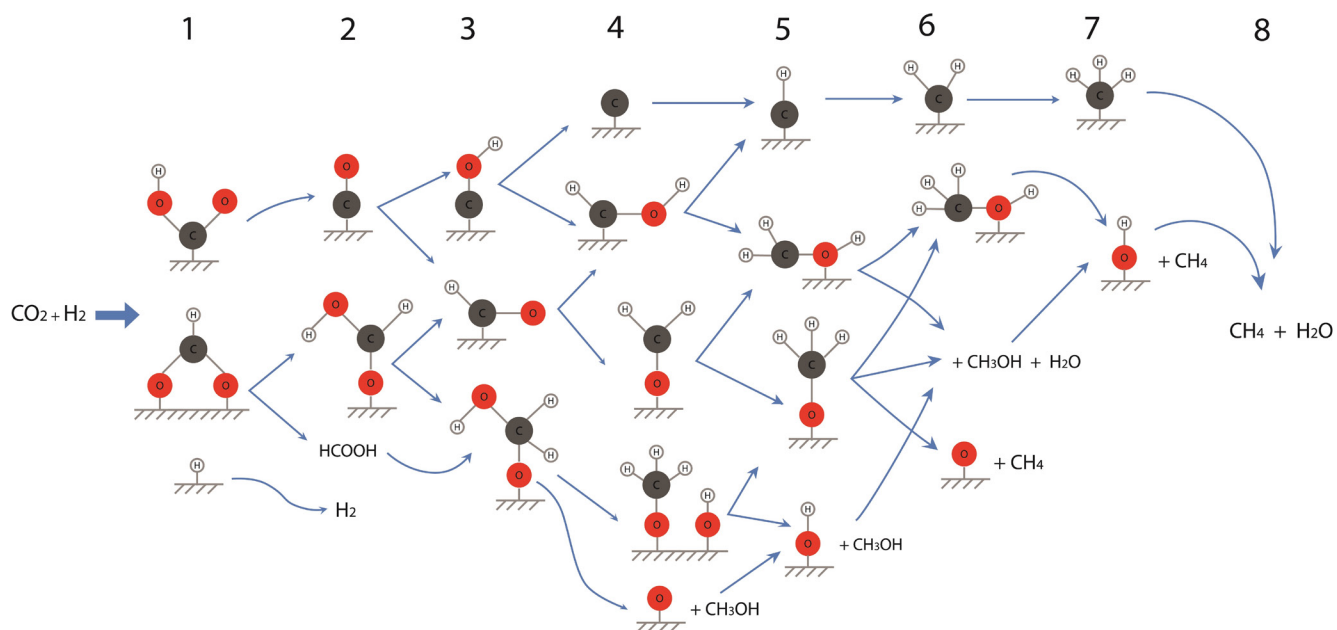

Figure 3: The CO2RR reaction network for 1C products. Electron transfer steps are indicated at the top.

Formic acid

Formic acid formation is a simple two step reaction with OCHO* as the surface bound species after the 1st proton transfer on oxide surfaces studied here. Rutile oxide surfaces follow the pathway with OCHO* due to the higher stability of OCHO* compared to COOH*. On metals, both the OCHO* mediated and the COOH* mediated pathway are observed[74]. OCHO* binds very strongly to all the oxide surfaces studied here and protonating it to release formic acid requires a reducing potential. The Ru-Ir mixed oxide system is on the left leg of the formic acid volcano and weaker binding surfaces are thus generally better at evolving formic acid. On the pure RuO_2(110) surface, it was predicted that very high CO* coverage weakens the OCHO* binding and produces formic acid at low overpotential[62]. At 75% CO* coverage, H* and OCHO* have similar binding free energies, however, and the HER dominate.

OCHO* binding free energy close to zero at 0 V-RHE leads to a low thermodynamic barrier for formic acid evolution. We find such optimal OCHO* binding with only 50% CO* coverage on surfaces with an active site based on an Ir atom but with Ru neighbors (discussed above) due to distinctive adsorbate binding behavior. On β=0.29 surface, with 50% CO* overage, OCHO* is 0.25 eV more stable than H* and the formic acid onset potential is -0.2 V-RHE (Table 4). Similar enhancement in the evolution of
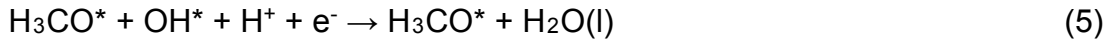
formic acid is observed for β=0.75. Thus, small amounts of Ir doping can enhance formic acid formation on RuO₂ and lowers the CO* coverage needed for moderate CO2RR onset potentials.

Table 4: Formic acid onset potential as a function of Ir-character of the oxide surface and CO coverage. Lightest share means highest value and darkest is the lowest value.*

β	0.00	0.05	0.11	0.25	0.29	0.75	0.79	0.90	0.95	1.00
CO* spectator coverage	Onset potential for formic acid evolution (V-RHE)									
0%	-0.71	-0.70	-0.70	-0.78	-0.84	-1.00	-1.05	-1.23	-1.14	-1.17
25%	-0.93	-0.97	-0.90	-1.02	-0.60	-0.45	-0.55	-1.13	-1.17	-1.13
50%	-0.60	-0.64	-0.67	-0.77	-0.20	-0.19	-0.44	-0.92	-1.09	-1.06

Methanol

A pure RuO_2 (110) surface reduces CO_2 to methanol by the following six electron pathway for 0% to 50% CO* coverage.

$$CO_2(aq) + H^+ + e^- + * \rightarrow OCHO* \qquad (1)$$
$$OCHO* + H^+ + e^- \rightarrow HCOOH* \text{ or } OCHO* + H^+ + e^- \rightarrow HCOOH \text{ (aq) } + * \qquad (2)$$
$$HCOOH* + H^+ + e^- \rightarrow H_2COOH* \text{ or } HCOOH(aq) + H^+ + e^- \rightarrow H_2COOH* \qquad (3)$$
$$H_2COOH* + H^+ + e^- \rightarrow H_3CO* + OH* \qquad (4)$$

$$H_3CO* + OH* + H^+ + e^- \rightarrow H_3CO* + H_2O(l) \qquad (5)$$

$$H_3CO* + H^+ + e^- \rightarrow H_3COH \text{ (aq) } + * \qquad (6)$$

For the Ir-Ru mixed oxide surfaces studied here, the 25% and 50% CO* coverage follows the same reaction pathway. Without CO* spectator, Ir-rich surfaces (β ≥ 0.75) prefer a methanol evolution pathway involving C-coordinated intermediates such as CHO* and CHOH*. However, an analysis of the potential determining step reveals that protonation of OCHO* to HCOOH* or an aqueous formic acid molecule, HCOOH(aq), still has the largest increase in free energy on most surfaces and most CO* coverages (Table 5). OCHO* is a very stable adsorbate and protonating it involves metal-oxygen bond breaking.

A few Ir-rich surfaces (β=0.95, 1.0) also show OH* removal or protonation of H_3CO* as onset potential determining step at CO* coverages of 25-50% and 25%, respectively. These surfaces need very high reducing potential due to the strong OH* binding nature of these Ir-rich surfaces. OH*, OCHO*, H_3CO* binding energies are correlated with each other as all three intermediates bind to the surface through oxygen atoms. Weak binding surfaces fails to bind HCOOH* and the formic acid molecules escape. However, the most active surfaces (e.g. β=0.29, 0.75) studied here bind H_2COOH* strongly and thus the formation of H_2COOH* from formic acid molecules is an energetically downhill process at 0 V-RHE. Quick removal of formic acid molecules will result in more formic acid production. However, with sufficient formic acid molecules

present in the electrolyte, methanol evolves. Thus, the final product mix would depend explicitly on the reaction conditions.

With 50% CO* coverage, Ir-overlayers and Ir substitution at bridge sites in the RuO_2 slab are predicted to evolve methanol at only -0.2 V-RHE, which is better than RuO_2 surface with optimized CO* coverage and any known metal catalyst[75,76]. In essence, using the surprising surface chemistry of the mixed Ir/Ru oxides and adsorbate-adsorbate interaction from CO* spectator, we can design very efficient oxide based methanol evolution catalysts.
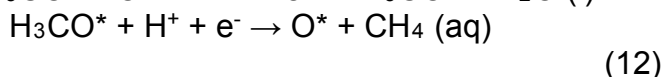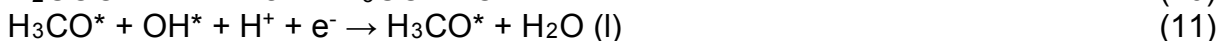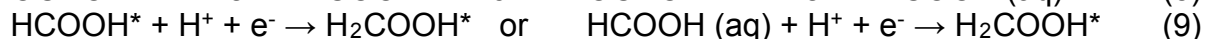
Table 5: Methanol evolution onset potential as a function of Ir-character of the oxide surface and CO coverage. Lightest share means highest value and darkest is the lowest value. The 2nd table provides the onset potential limiting step for each surface and CO* coverage combination.*

β	0.00	0.05	0.11	0.25	0.29	0.75	0.79	0.90	0.95	1.00
CO* spectator coverage	Onset potential for methanol evolution (V-RHE)									
0%	-0.71	-0.70	-0.70	-0.78	-0.78	-0.79	-1.05	-0.93	-0.83	-0.81
25%	-0.77	-0.75	-0.75	-0.80	-0.60	-0.45	-0.55	-0.82	-0.93	-0.93
50%	-0.46	-0.46	-0.54	-0.54	-0.20	-0.20	-0.44	-0.92	-0.92	-1.07

B	0.00	0.05	0.11	0.25	0.29	0.75	0.79	0.90	0.95	1.00
CO* spectator coverage	Potential determining step for methane evolution									
0%	OCHO* protonation	OCHO* protonation	OCHO* protonation	OCHO* protonation	OCHO* protonation	OCHO* protonation	OCHO* protonation	OCHO* protonation	OCHO* protonation	OCHO* protonation
25%	OCHO* protonation	OCHO* protonation	OCHO* protonation	OCHO* protonation	OCHO* protonation	OCHO* protonation	OCHO* protonation	H3CO* protonation	OH* removal	OH* removal
50%	OCHO* protonation	OCHO* protonation	OCHO* protonation	OCHO* protonation	OCHO* protonation	OCHO* protonation	OCHO* protonation	OCHO* protonation	OH* removal	OCHO* protonation

Methane

With some CO* coverage, all mixed oxide surfaces follow a methane evolution path consisting of oxygen coordinated intermediates as follows:

CO_2(aq) + H^+ + e^- + * → OCHO* $\qquad$ (7)

OCHO* + H^+ + e^- → HCOOH* $\quad$ or $\quad$ OCHO* + H^+ + e^- → HCOOH (aq) + * $\quad$ (8)

HCOOH* + H^+ + e^- → H_2COOH* $\quad$ or $\quad$ HCOOH (aq) + H^+ + e^- → H_2COOH* $\quad$ (9)

H_2COOH* + H^+ + e^- → H_3CO* + OH* $\qquad$ (10)

H_3CO* + OH* + H^+ + e^- → H_3CO* + H_2O (l) $\qquad$ (11)

H_3CO* + H^+ + e^- → O* + CH_4 (aq)

$$(12)$$

O* + H^+ + e^- → OH* $\qquad$ (13)

OH* + H^+ + e^- → H_2O(l) + * $\qquad$ (14)

For this pathway, OH* removal or OCHO* protonation requires the largest onset potential (Table 6). After the 5th reaction step, a H_3CO* intermediate is formed. At the 6th electron transfer step, protonation at the carbon atom in the H_3CO* intermediate leads to release of methane.

In the absence of CO* spectators, Ir-rich surfaces (β=0.9, 0.95, 1.0) bind carbon coordinated adsorbates very strongly. Thus, on such surfaces, adsorbates like CH*, CHOH*, CHO*, CH_2*, CH_3* participates in the reaction mechanism. Despite this, OCHO* protonation remains the most energetically difficult reaction step. The OCHO* adsorption energy scales with the OH* binding energy and the weakest OH* binding surfaces, β = 0.29 or β = 0.75, shows the lowest methane evolution overpotential at 50% CO* coverage.

Ir-oxide overlayers on RuO_2 display a methanol onset potential of -0.45 V-RHE with only 25% CO* coverage. For the pure RuO_2 surface, with 50% CO* coverage a similar onset potential of -0.46 V-RHE is predicted (methanol onset potential computed in this work can change due to the difference in assumed concentration of methanol in solution[62]). Thus, the OCHO* protonation step dictates the onset potential to be -0.45 V-RHE.

Table 6: Methane evolution onset potential as a function of Ir-character of the oxide surface and CO coverage. Lightest share means highest value and darkest is the lowest value. The 2nd table provides the onset potential determining step for each surface and CO* coverage combination.*

β	0.00	0.05	0.11	0.25	0.29	0.75	0.79	0.90	0.95	1.00
CO* spectator coverage	Onset potential for methane evolution (V-RHE)									
0%	-0.71	-0.70	-0.70	-0.79	-0.78	-0.79	-1.05	-0.93	-0.89	-0.81
25%	-0.77	-0.75	-0.75	-0.80	-0.60	-0.52	-0.55	-0.97	-1.12	-1.10
50%	-0.47	-0.57	-0.54	-0.63	-0.30	-0.36	-0.44	-0.94	-1.05	-1.07

β	0.00	0.05	0.11	0.25	0.29	0.75	0.79	0.90	0.95	1.00
CO* spectator coverage	Potential determining step for methane evolution									
0%	OCHO* protonation	OCHO* protonation	OCHO* protonation	OH* removal	OCHO* protonation	OCHO* protonation	OCHO* protonation	OCHO* protonation	OH*removal	OCHO* protonation
25%	OCHO* protonation	OCHO* protonation	OCHO* protonation	OCHO* protonation	OCHO* protonation	OH*removal	OCHO* protonation	OH*removal	OH*removal	OH*removal
50%	OH*removal	OH*removal	OCHO* protonation	OH*removal	OH*removal	OH*removal	OCHO* protonation	OH*removal	OH*removal	OCHO* protonation

Scaling of binding energies with CO* spectator coverage

The CO* spectator interactions with CO2RR adsorbates are found to be both attractive and repulsive, as exemplified through the binding energy variation of OH*/H*/CO* with CO* coverage. A thermodynamic analysis of the reaction pathways reveals that OH* removal, OCHO* activation, or H_3CO* protonation to methanol determine the onset potential of the CO2RR reaction for different composition and CO* coverages. Because all these adsorbates are bound to the surfaces through oxygen, an increase in the OH* binding strength leads to stronger OCHO* and H_3CO* binding as well. Indeed, when we plot the binding energy of OCHO* and H_3CO* (Figure 4), a strong interdependency is observed.

Adsorbates, which have common central atom engaging in chemical bond formation with catalyst surface, often have binding energy, which correlates strongly with each other. These observed linear relations between the binding energy of such adsorbates are known as scaling laws in catalysis[77]. Due to the similarity in chemical nature of RuO_2 and IrO_2, the spread in binding energy observed for the 10 model surfaces is narrow and lead to large error in linear fit for scaling laws with data presented in this work.

Interestingly, for the H3CO*-OH* adsorbate binding free energy correlation, the three scaling lines drawn based on linear fitting of data points from three different CO* coverage, follow each other closely with a slope of 1 (slope m=1.02, 1.11, 1.08 for 0%, 25%, 50% CO* coverage respectively) and an offset depending on the CO* coverage.

This result is in good agreement with previously reported H3CO*-OH* scaling line on rutile oxides with a slope of 0.96[21].

For the OCHO*-OH* scaling, computed slopes are m=1.29, 0.84, 0.89, respectively, for 0%, 25%, 50% CO* coverage, indicating that the chemical nature of the scaling relation changes if CO* coverage is considered. OCHO* is bidentate and binds through one bridge and one cus site. The scaling line slope for 25% CO* coverage deviates from the slope of 0.99 calculated in previous theoretical work which considers 25% CO* coverage. The slope of 0.99 was derived from binding energies observed on rutile oxide surfaces with identical bridge and cus elements and a much wider variety of binding characteristics[21]. The rather small variation in chemical nature of the surfaces considered here compared to those studied previously result in skewed data and a different estimate of the slope. The quality of fit for scaling lines is better for OH*/H$_3$CO* binding free energy correlation than between OH*/OCHO*. The chemical origin of observed scaling relation between two adsorbates is based on the similar nature of bonding with the catalyst surface, where OH* and H$_3$CO* binding through one oxygen atom to the bridge site, OCHO* binding through two oxygen atoms at one bridge and adjoining cus site. Thus, it is possible to have different coordinating metal atoms at the cus site, while bridge site character remains unchanged on a mixed oxide surface. Also, CO* adsorbates affect cus and bridge site binding differently. Disparate effects at bridge and cus site create larger scatter in OH*/OCHO* scaling line.

Even with the variation in scaling line from CO* coverage effects, the fundamental behavior remains unperturbed. This indicates that a universal adsorbate scaling relation for O-coordinates adsorbates on rutile oxide surface exist, which holds irrespective of the CO* coverage, but with a CO* coverage dependent offset. This unification can help to model CO2RR activity on oxide catalysts without simulating the full thermodynamic path. The OH* binding energy at different CO* coverage can provide onset potential for the key reaction steps.
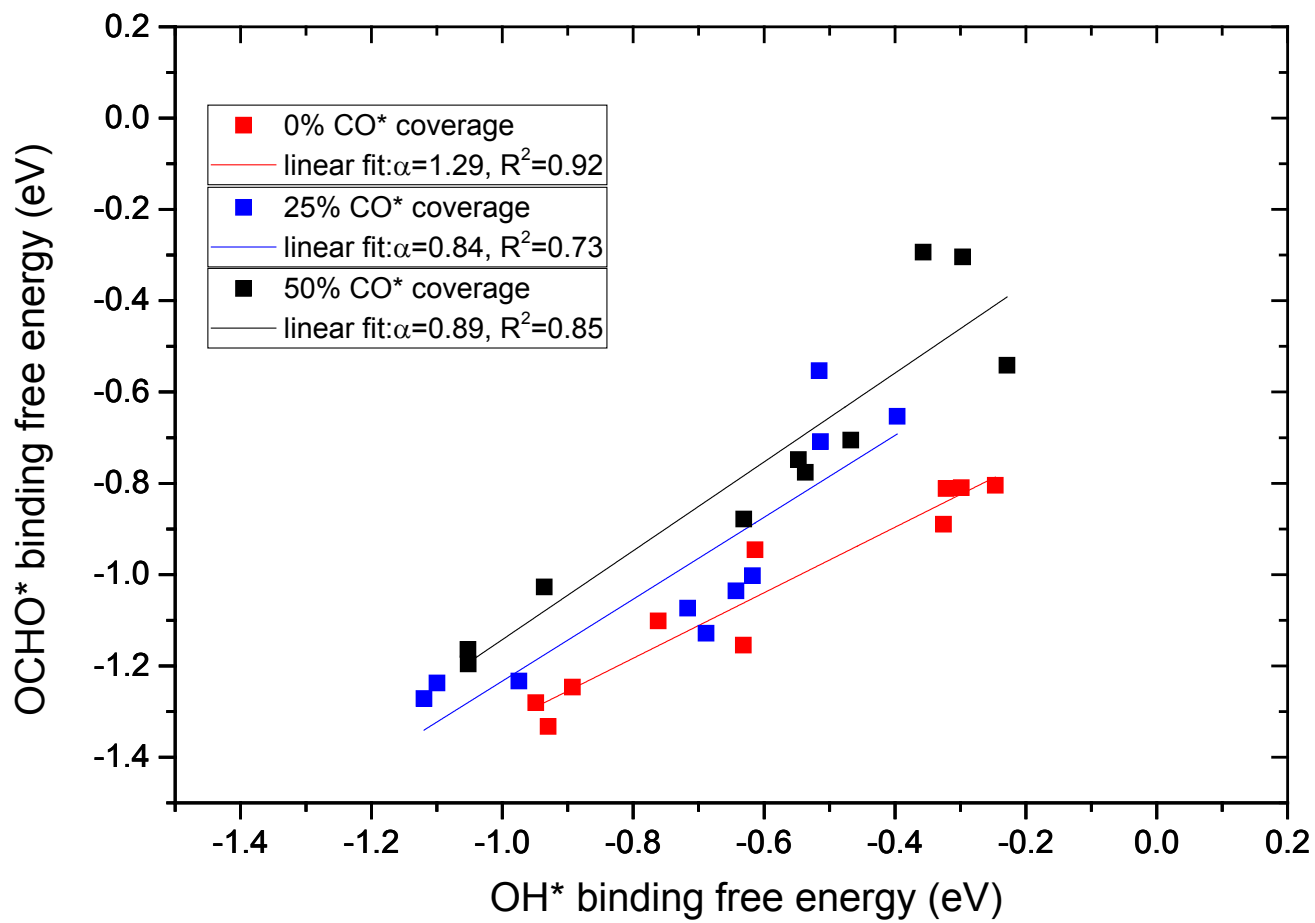
(a)
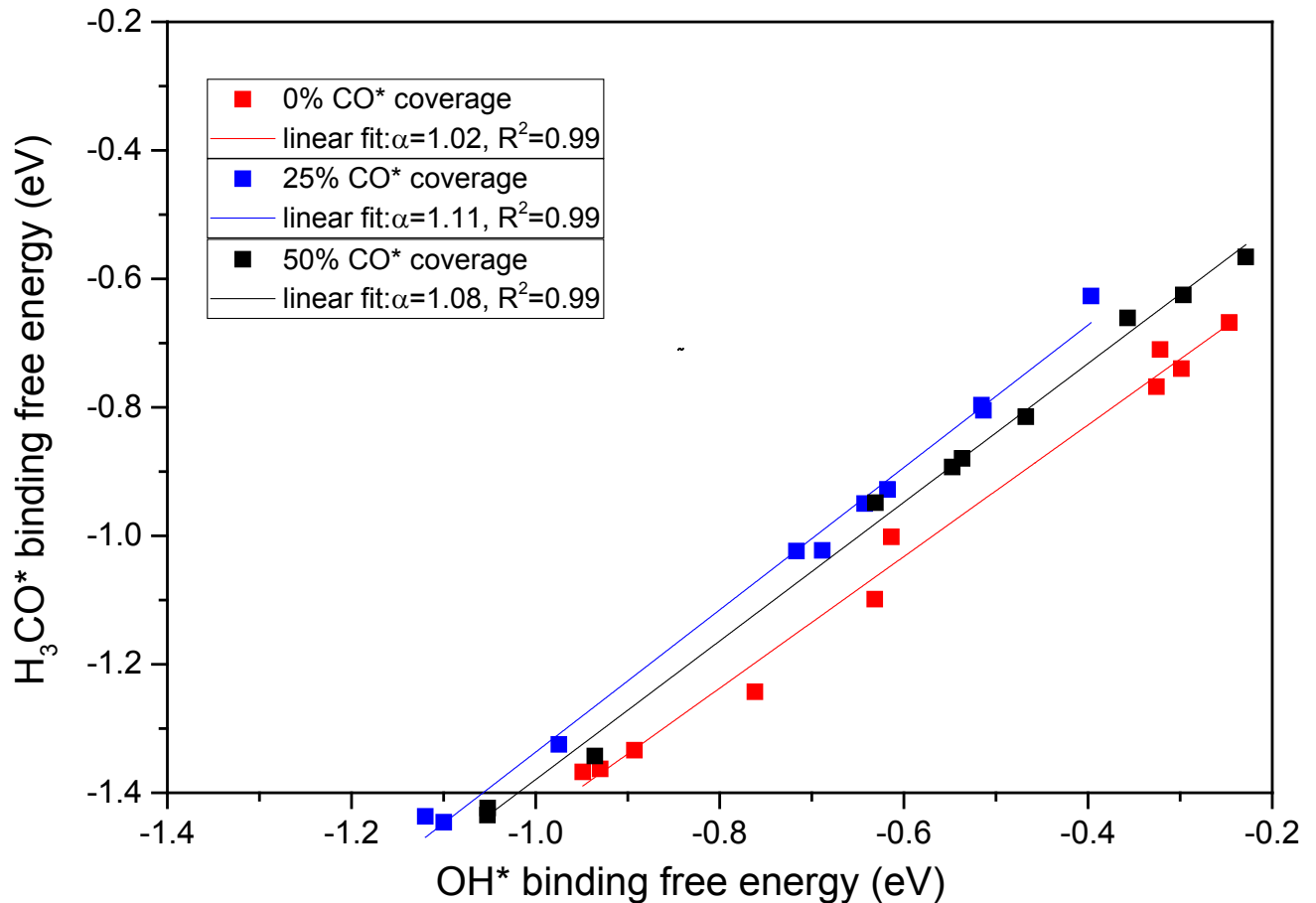
(b)

Figure 4: (a) OCHO*-OH* and (b) H_3CO^* - OH* binding free energy scaling relation at three different CO* coverages with slope α and coefficient of determination R^2.

Electronic structure effects in mixed oxide surfaces

Adsorbate binding properties and thus the catalytic activities of oxides have previously been shown to depend on the oxygen atom *p*-band position[78,79] and the metal atom *d*-band configuration[80,81]. RuO_2, IrO_2 and their mixed oxides show strong metal oxygen overlap covalency[82,83] and any modification in the atomistic constituent will thus affect both the O-*p* and metal-*d* band. The effects of such changes on adsorbate binding are therefore expectedly also coupled.

Here, we have computed the *d*-band center for the two metal atoms constituting the bridge site on all surfaces and with all coverages (Figure S5 and S6). The calculation is also done for the average *p*-band center for the O atoms in the top layer of the catalyst surfaces, for a trend analysis (Figure S5 and S6). Here, the binding energy of the key adsorbate OH* (activity descriptor) is found to be not correlated singularly with either metal d-band or oxygen p-band position (Figure S5).

A Bader charge[84] analysis for these metal and oxygen atoms reveals that the oxidation number of oxygen does not change significantly with the metal atom present or with the CO* coverage (Table 7). In comparison with Ru atoms at the bridge site in the pure RuO_2 surface, the Ru atoms at the bridge site in mixed oxide surfaces with Ir atoms as neighbors do not show large deviation in oxidation number. On the contrary, bridge site constituting Ir atoms that have Ru neighbors (β= 0.29, 0.75, 0.79) show markedly reduced oxidation number especially with CO* spectators (Table 7) compared to surfaces with $\beta \geq 0.8$. OH* is an electron accepting adsorbate. A lower oxidation state of the metal atom would prevent the formation of a strong bond to OH via electron exchange. The correlation between the charge state of the metal atoms closest to the bridge site and OH* binding energy is evident from the correlation plot in Figure 5, where two distinct correlations emerge. Up to a Bader oxidation number of 1.2 for metal atoms constituting bridge site, OH* binding strength weakens sharply with increase in oxidation number. This regime correlation is populated by all surfaces without CO* coverage and CO* covered surfaces with β=0.29, 0.75, 0.79. Beyond a value of 1.2, OH* binding weakens slowly with higher oxidation number starting from OH* binding free energy of -1.15 eV. This regime is populated by CO* covered surfaces with β=0.0, 0.11, 0.25, 0.90, 0.95, 1.0.

CO* adsorbates transfer charge to the metal atom through covalent bonding when adsorbing onto an oxide surface[85]. Surfaces with low or high β change regime with an increase in oxidation number due to electron doping by the CO* spectators. It is striking to notice that Ru-Ir ligand interaction in surfaces with β=0.29, 0.75, 0.79, prevents electron donation from CO* to increase metal oxidation number to increase significantly. These surfaces remain on the same correlation regime of OH* binding and Bader charge dependency, leading to much weaker OH* binding.

Even in the absence of any strain effect and without any CO* spectators, a wide variation in band centers (Figure SI6) is observed for both Ir and Ru atoms next to the bridge site and the oxygen atoms close to them. The range of band positions observed in the mixed oxide surfaces ranges both above and below the band position of the metal-d band and the O-p band of pure IrO_2 and RuO_2, strongly indicating that complex non-linear ligand effects are in play. It is clear that ligand effects between the chemically similar Ir and Ru atoms are strong and result in electronic structure modification leading to anomalous behavior in the mixed oxides. The presence of CO* spectators (electron donors) further enhances this unprecedented behavior. These findings show that mixed oxide catalyst design should explicitly include the electronic structure effects due to metal-metal ligand interaction through the oxygen p-band.

Here, such interaction leads to changes in the band positions. For Ir atoms in the oxide electrocatalysts, t_{2g} orbitals are occupied and e_g orbitals are empty[86]. Due to interaction with neighboring Ru atoms, the Ir-atom t_{2g} orbital changes position. For β=0.29, the Ir atom has only Ru neighbors. Its t_{2g} orbital increases in energy without CO* coverage, compared to active site Ir atom in pure IrO_2. With CO* coverage, the shift is in opposite direction. β=0.75 surface has both Ir and Ru atoms as neighbors and the Ir atoms' t_{2g} orbital shifts even more in the negative direction when CO* spectators are present (Figure 6). A negative shift of d-orbital causes weaker binding with the O-2p orbital of adsorbate[87].

Due to the strong covalency of the oxide, oxygen p-orbital gets affected as well. Differences originating from both the oxygen and metal atom electronic structure parameters affect the adsorbate binding energy. The intricacy of the intermingled effects results in a complex, non-linear correlation with the adsorbate binding energy, which is beyond the scope of the model systems under consideration here. Blocking of Kramers Anderson super-exchange in metal-oxygen-metal bond due to onsite triplet pairing at ruthenium t_{2g} orbital might be crucial, although this is speculative as magnetic effects are not included in this work. Detailed analysis is currently ongoing. The lack of simple correlations of binding energy with either metal-d or oxygen-p band center position parameter is provided in the supplementary information.

Table 7: Oxidation number of metal atom 1 (ON1) and atom 2 (ON2) that make up the bridge site and average oxidation number of oxygen atoms in the top layers calculated from Bader charges. Yellow boxes for Ru-atom and green boxes for Ir atom.

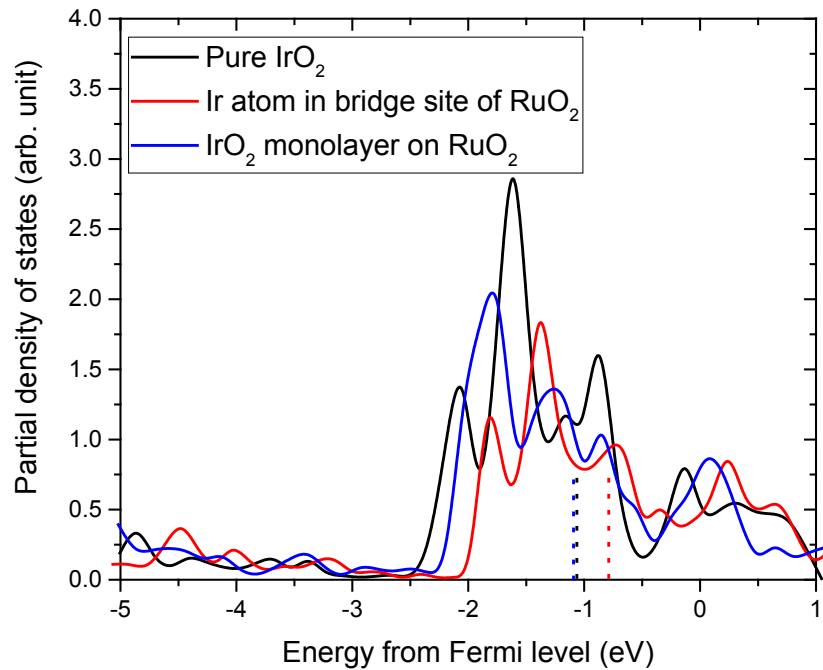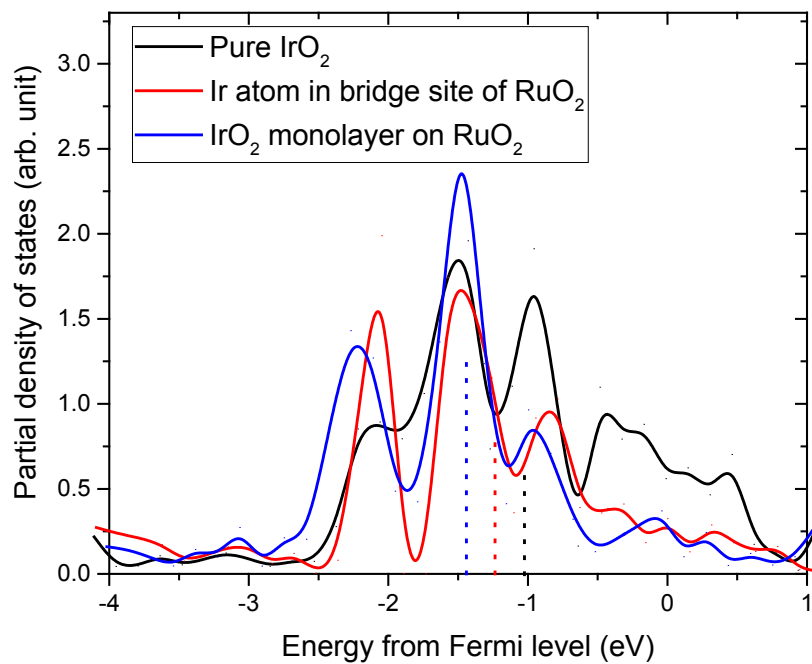| β	0% CO* coverage			25% CO* coverage			50% CO* coverage		
	ON1	ON2	ON-oxygen	ON1	ON2	ON-oxygen	ON1	ON2	ON-oxygen
0.00	1.19	1.21	-0.87	1.30	1.30	-0.85	1.33	1.33	-0.84
0.05	1.18	1.20	-0.87	1.28	1.29	-0.85	1.32	1.32	-0.84
0.11	1.20	1.20	-0.86	1.30	1.30	-0.84	1.31	1.30	-0.84
0.25	1.19	1.19	-0.86	1.29	1.29	-0.85	1.32	1.31	-0.85
0.29	1.20	1.12	-0.86	1.32	1.02	-0.85	1.36	1.01	-0.84
0.75	1.16	1.16	-0.85	1.28	1.06	-0.85	1.29	1.06	-0.85
0.79	1.22	1.11	-0.85	1.33	1.03	-0.85	1.35	1.00	-0.87
0.9	1.16	1.16	-0.86	1.23	1.23	-0.84	1.23	1.22	-0.84
0.95	1.16	1.16	-0.85	1.21	1.21	-0.85	1.20	1.21	-0.86
1.00	1.14	1.14	-0.85	1.21	1.21	-0.85	1.21	1.21	-0.87
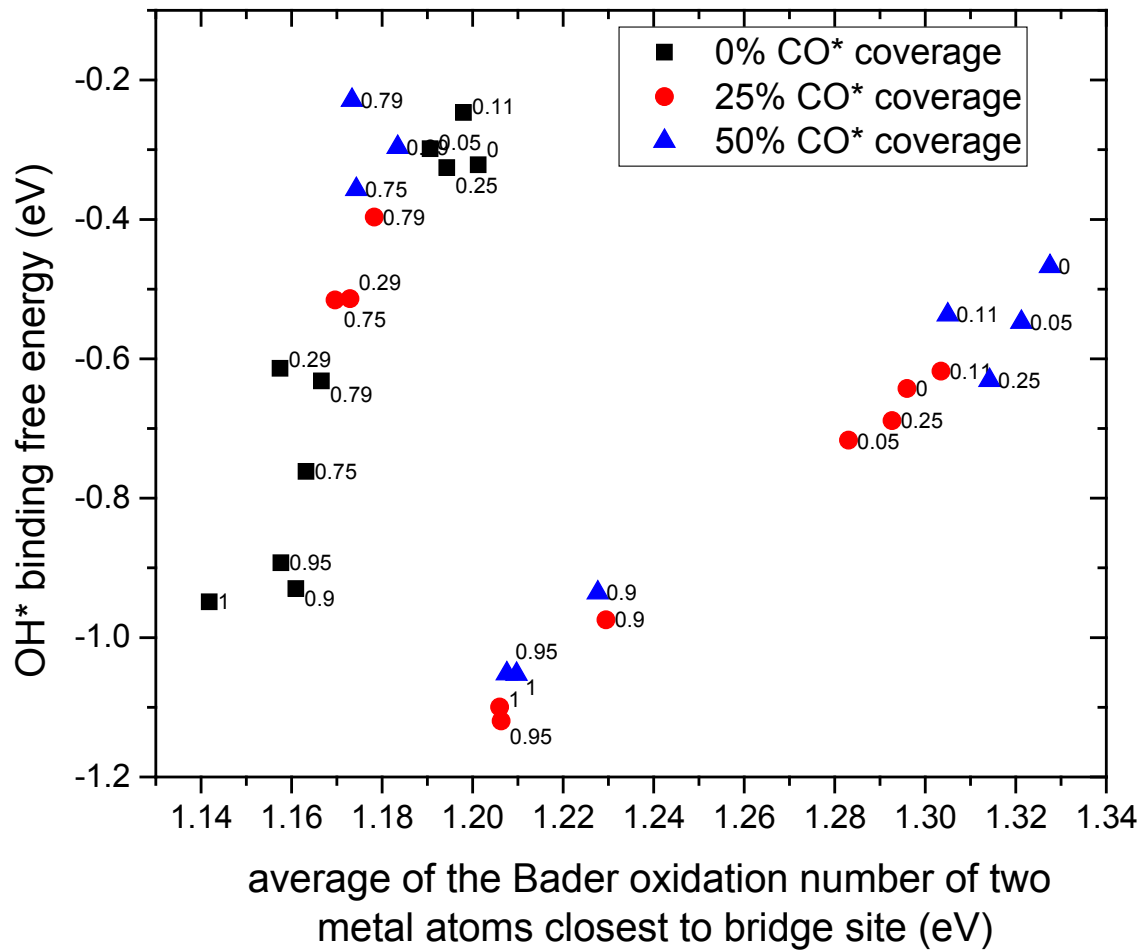
Figure 5: Correlation of OH* binding free energy with average Bader oxidation number of the two metal atoms at the bridge site. Labels indicate the β value of the surface for which the data point.

(a)

(b)

Figure 6: Shift in the t_{2g} orbital of Ir atom from ligand effect of neighboring ruthenium atom, (a) no CO* coverage (b) 50% CO* coverage. t_{2g} band centers for Ir atom is marked.

Conclusion

RuO$_2$-based CO2RR electrocatalysts hold great promise for conversion of CO2 into liquid fuel. The overpotential and selectivity of these catalysts can be further enhanced through control of the CO* coverage and more importantly through doping with Ir. In the presence of CO* and OH* spectators (often present under CO2RR conditions), small amounts of Ir substituents are predicted to segregate near the bridge position in rutile (110) surface.

Bridge sites in surfaces with β=0.29, 0.75 or 0.79 show intriguing non-linear adsorbate binding energies, due to strong ligand effects from neighboring Ru atoms onto the Ir atom constituting the bridge site. CO* binds much stronger on surfaces with such bridge sites than on the pure IrO$_2$ and RuO$_2$ oxides. The CO* adsorbate interaction effects are also more influential for these mixed oxide surfaces, where, e.g., the CO* interaction leads to weaker OCHO* and OH* binding on these surfaces.

A thermodynamic reaction pathway analysis shows two elementary steps determine the onset potential for CO2RR regardless of the chemical nature of the bridge site and CO* spectator coverage - (a) OCHO* protonation (b) OH* removal. The CO* interaction weakens the binding energy of OH* for β=0.75 or β=0.29 such that an onset potential for methanol of -0.2 V-RHE is predicted.

We also have shown the universality of OH*/OCHO* and OH*/H$_3$CO* scaling relations regardless of CO* coverage, simplifying the analysis of CO2RR activity on CO* coverage mixed oxide systems. Enhancements of the catalytic activity in mixed oxides come from a concerted ligand and spectator effects, where mixing of oxides with strong covalent character can lead to remarkable electronic structure effects and binding energy behavior. Through these synergistic effects, activity for electrochemical conversion of CO$_2$ into liquid fuel is improved by moving closer to the top of the activity volcano[21] for different products on oxide catalysts predicted previously (Figure 7 and S7). This new concept of ligand effect based manipulation of adsorbate binding can open a door to novel avenues of catalyst engineering e.g. for oxygen evolution. Ligand effects in oxides catalysts are unexplored and this work indicates to the immense possibility in that.
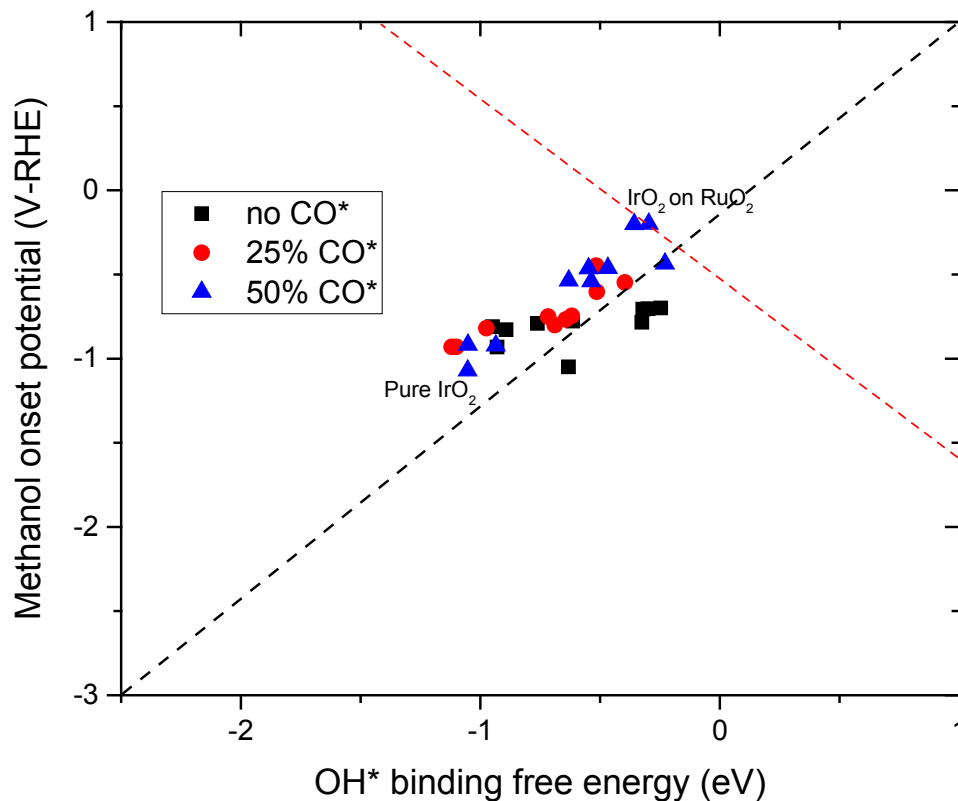
Figure 7: synergistic effects from ligand interaction and adsorbate-adsorbate interaction from spectating CO* moves partially CO* covered mixed Ir-Ru oxide surfaces closer to the top of the volcano for methanol evolution on oxide catalysts. Activity volcanos for different products obtained from our previous work[21].

Unlike metals, where simple interpolation techniques often provide good approximations of the binding energies of key adsorbates, mixed oxides display a more complex electronic structure variations. The increased complexity also provides a unique possibility to design very active catalysts with low levels of cation substitution. Specifically, we propose a monolayer or less of IrO_2 deposited on the RuO_2 (110) surface to be a very good CO2RR catalyst for formic acid and methanol evolution with moderate CO* coverage.

Supporting Information

Additional explanation for computational methods, visualizations for adsorbate configurations, free energy plot for all adsorbates on all surfaces and CO* coverages, correlation of β, OH* binding and important electronic structure parameters are provided in supporting information section.

Acknowledgements

References:

(1)   Lewis, N. S.; Nocera, D. G. *Proc. Natl. Acad. Sci.* **2006**, *103*, 15729–15735.

(2)   Olah, G. A.; Goeppert, A.; Prakash, G. K. S. *Beyond Oil and Gas: The Methanol Economy*; Wiley-VCH Verlag GmbH & Co. KGaA: Weinheim, Germany, 2009.

(3)   Chu, S.; Cui, Y.; Liu, N. *Nat. Mater.* **2016**, *16*, 16–22.

(4)   Ganesh, I. *Renew. Sustain. Energy Rev.* **2014**, *31*, 221–257.

(5)   Centi, G.; Perathoner, S. *Catal. Today* **2009**, *148*, 191–205.

(6)   Whipple, D. T.; Kenis, P. J. A. *J. Phys. Chem. Lett.* **2010**, *1*, 3451–3458.

(7)   Hori, Y.; Kikuchi, K.; Suzuki, S. *Chem. Lett.* **1985**, *14*, 1695–1698.

(8)   Hori, Y.; Murata, A.; Takahashi, R. *J. Chem. Soc. Faraday Trans. 1 Phys. Chem. Condens. Phases* **1989**, *85*, 2309.

(9)   Hori, Y. In *Modern Aspects of Electrochemistry*; Springer New York, 2008; Vol. 42, pp 89–189.

(10) Peterson, A. A.; Abild-Pedersen, F.; Studt, F.; Rossmeisl, J.; Nørskov, J. K.; Lewis, N. S.; Nocera, D. G.; Hori, Y.; Kikuchi, K.; Murata, A.; Suzuki, S.; Hori, Y.; Murata, A.; Takahashi, R.; Suzuki, S.; Kim, J. J.; Summers, D. P.; Jr, K. W. F.; Cook, R. L.; MacDuff, R. C.; Sammells, A. F.; DeWulf, D. W.; Jin, T.; Bard, A. J.; Hori, Y.; Murata, A.; Takahashi, R.; Hori, Y.; Wakebe, H.; Tsukamoto, T.; Koga, O.; Jesús-Cardona, H. De; Moral, C. del; Cabrera, C. R.; Delacourt, C.; Ridgway, P. L.; Kerr, J. B.; Newman, J.; Gattrell, M.; Gupta, N.; Co, A.; Janik, M. J.; Taylor, C. D.; Neurock, M.; Blum, L.; Huckaby, D. A.; Marzari, N.; Car, R.; Zhang, T.; Anderson, A. B.; Koper, M. T. M.; Roudgar, A.; Groß, A.; Fang, Y.-H.; Liu, Z.-P.; Adriaanse, C.; Sulpizi, M.; VandeVondele, J.; Sprik, M.; Wang, G.-C.; Jiang, L.; Morikawa, Y.; Nakamura, J.; Cai, Z.-S.; Pan, Y.-M.; Zhao, X.-Z.; Au, C. T.; Chen, M. D.; Schumacher, N.; Andersson, K.; Grabow, L.; Mavrikakis, M.; Nerlov, J.; Chorkendorff, I.; Gokhale, A. A.; Dumesic, J. A.; Mavrikakis, M.; Rossmeisl, J.; Skúlason, E.; Björketun, M. E.; Tripkovic, V.; Nørskov, J. K.; Nørskov, J. K.; Rossmeisl, J.; Logadottir, A.; Lindqvist, L.; Kitchin, J. R.; Bligaard, T.; Jonsson, H.; Tripkovic, V.; Skúlason, E.; Siahrostami, S.; Nørskov, J. K.; Rossmeisl, J.; N?rskov, J. K.; Nørskov, J. K.; Lewis, N. S.; Nocera, D. G.; Hori, Y.; Kikuchi, K.; Murata, A.; Suzuki, S.; Hori, Y.; Murata, A.; Takahashi, R.; Suzuki, S.; Kim, J. J.; Summers, D. P.; Jr, K. W. F.; Cook, R. L.; MacDuff, R. C.; Sammells, A. F.; DeWulf, D. W.; Jin, T.; Bard, A. J.; Hori, Y.; Murata, A.; Takahashi, R.; Hori, Y.; Wakebe, H.; Tsukamoto, T.; Koga, O.; Jesús-Cardona, H. De; Moral, C. del; Cabrera, C. R.; Delacourt, C.; Ridgway, P. L.; Kerr, J. B.; Newman, J.; Gattrell,

M.; Gupta, N.; Co, A.; Janik, M. J.; Taylor, C. D.; Neurock, M.; Blum, L.; Huckaby, D. A.; Marzari, N.; Car, R.; Zhang, T.; Anderson, A. B.; Koper, M. T. M.; Roudgar, A.; Groß, A.; Fang, Y.-H.; Liu, Z.-P.; Adriaanse, C.; Sulpizi, M.; VandeVondele, J.; Sprik, M.; Wang, G.-C.; Jiang, L.; Morikawa, Y.; Nakamura, J.; Cai, Z.-S.; Pan, Y.-M.; Zhao, X.-Z.; Au, C. T.; Chen, M. D.; Schumacher, N.; Andersson, K.; Grabow, L.; Mavrikakis, M.; Nerlov, J.; Chorkendorff, I.; Gokhale, A. A.; Dumesic, J. A.; Mavrikakis, M.; Rossmeisl, J.; Skúlason, E.; Björketun, M. E.; Tripkovic, V.; Nørskov, J. K.; Nørskov, J. K.; Rossmeisl, J.; Logadottir, A.; Lindqvist, L.; Kitchin, J. R.; Bligaard, T.; Jonsson, H.; Tripkovic, V.; Skúlason, E.; Siahrostami, S.; Nørskov, J. K.; Rossmeisl, J. *Energy Environ. Sci.* **2010**, *3*, 1311.

(11) Peterson, A. A.; Nørskov, J. K. *J. Phys. Chem. Lett.* **2012**, *3*, 251–258.

(12) Hansen, H. A.; Varley, J. B.; Peterson, A. A.; Nørskov, J. K. *J. Phys. Chem. Lett.* **2013**, *4*, 388–392.

(13) Li, Y.; Sun, Q. *Adv. Energy Mater.* **2016**, *6*, 1–19.

(14) Bandi, A.; Kiihne, H. *J. Electrochem. Soc.* **1992**, *139*, 1605.

(15) Bandi, A. *J. Electrochem. Soc.* **1990**, *137*, 2157.

(16) Popic, J. P.; Avramov-Ivic, M. L.; Vukovic, N. B.; Popić, J.; Avramov-Ivić, M.; Vuković, N.; Popic, J. P.; Avramov-Ivic, M. L.; Vukovic, N. B.; Popić, J.; Avramov-Ivić, M.; Vuković, N. *J. Electroanal. Chem.* **1997**, *421*, 105–110.

(17) Qu, J.; Zhang, X.; Wang, Y.; Xie, C. *Electrochim. Acta* **2005**, *50*, 3576–3580.

(18) Spataru, N.; Tokuhiro, K.; Terashima, C.; Rao, T. N.; Fujishima, A. *J. Appl. Electrochem.* **2003**, *33*, 1205–1210.

(19) Rochefort, D.; Dabo, P.; Guay, D.; Sherwood, P. M. A. *Electrochim. Acta* **2003**, *48*, 4245–4252.

(20) Kasian, O.; Geiger, S.; Stock, P.; Polymeros, G.; Breitbach, B.; Savan, A.; Ludwig, A.; Cherevko, S.; Mayrhofer, K. J. J. *J. Electrochem. Soc.* **2016**, *163*, F3099–F3104.

(21) Bhowmik, A.; Vegge, T.; Hansen, H. A. *ChemSusChem* **2016**, *9*, 3230–3243.

(22) Karamad, M.; Hansen, H. A.; Rossmeisl, J.; Nørskov, J. K. *ACS Catal.* **2015**, *5*, 4075–4081.

(23) Jacobsen, C. J. H.; Dahl, S.; Clausen, B. S.; Bahn, S.; Logadottir, A.; Nørskov, J. K. *J. Am. Chem. Soc.* **2001**, *123*, 8404–8405.

(24) Studt, F.; Sharafutdinov, I.; Abild-Pedersen, F.; Elkjær, C. F.; Hummelshøj, J. S.; Dahl, S.; Chorkendorff, I.; Nørskov, J. K. *Nat. Chem.* **2014**, *6*, 320–324.

(25) Stoerzinger, K. A.; Qiao, L.; Biegalski, M. D.; Shao-Horn, Y. *J. Phys. Chem. Lett.* **2014**, *5*, 1636–1641.

(26) Stoerzinger, K. A.; Diaz-Morales, O.; Kolb, M.; Rao, R. R.; Frydendal, R.; Qiao, L.;

Wang, X. R.; Halck, N. B.; Rossmeisl, J.; Hansen, H. A.; Vegge, T.; Stephens, I. E. L.; Koper, M. T. M.; Shao-Horn, Y. *ACS Energy Lett.* **2017**, *2*, 876–881.

(27) Rossmeisl, J.; Qu, Z. W.; Zhu, H.; Kroes, G. J.; Nørskov, J. K. *J. Electroanal. Chem.* **2007**, *607*, 83–89.

(28) Angelinetta, C.; Trasatti, S.; Atanasoska, L. D.; Minevski, Z. S.; Atanasoski, R. T. *Mater. Chem. Phys.* **1989**, *22*, 231–247.

(29) Marshall, A. T.; Haverkamp, R. G. *Electrochim. Acta* **2010**, *55*, 1978–1984.

(30) Lyons, M. E. G.; Floquet, S. *Phys. Chem. Chem. Phys.* **2011**, *13*, 5314–5335.

(31) Kötz, R.; Stucki, S. *Electrochim. Acta* **1986**, *31*, 1311–1316.

(32) Siahrostami, S.; Vojvodic, A. *J. Phys. Chem. C* **2015**, *119*, 1032–1037.

(33) Cheng, J.; Zhang, H.; Chen, G.; Zhang, Y. *Electrochim. Acta* **2009**, *54*, 6250–6256.

(34) Lee, Y.; Suntivich, J.; May, K. J.; Perry, E. E.; Shao-Horn, Y. *J. Phys. Chem. Lett.* **2012**, 3, 399–404.

(35) Over, H.; Seitsonen, A. P.; Lundgren, E.; Schmid, M.; Varga, P. *J. Am. Chem. Soc.* **2001**, *123*, 11807–11808.

(36) Lister, T. E.; Tolmachev, Y. V.; Chu, Y.; Cullen, W. G.; You, H.; Yonco, R.; Nagy, Z. *J. Electroanal. Chem.* **2003**, *554–555*, 71–76.

(37) Doyle, A. D.; Montoya, J. H.; Vojvodic, A. *ChemCatChem* **2015**, *7*, 738–742.

(38) Toftelund, A.; Man, I. C.; Hansen, H. A.; Abild-Pedersen, F.; Bligaard, T.; Rossmeisl, J.; Studt, F. *ChemCatChem* **2012**, *4*, 1856–1861.

(39) Torun, E.; Fang, C. M.; De Wijs, G. A.; De Groot, R. A. *J. Phys. Chem. C* **2013**, *117*, 6353–6357.

(40) Gutsche, C.; Moeller, C. J.; Knipper, M.; Borchert, H.; Parisi, J.; Plaggenborg, T. *J. Phys. Chem. C* **2016**, *120*, 1137–1146.

(41) Wang, H. Y.; Schneider, W. F. *Mol. Simul.* **2012**, *38*, 615–630.

(42) Wang, J.; Fan, C. Y.; Jacobi, K.; Ertl, G. *Surf. Sci.* **2001**, *481*, 113–118.

(43) Karlsson, R. K. B.; Cornell, A.; Pettersson, L. G. M. *J. Phys. Chem. C* **2016**, *120*, 7094–7102.

(44) Xu, J. H.; Jarlborg, T.; Freeman, A. J. *Phys. Rev. B* **1989**, *40*, 7939–7947.

(45) Butler, S. R.; Gillson, J. L. *Mater. Res. Bull.* **1971**, *6*, 81–89.

(46) Mavrikakis, M.; Hammer, B.; Nørskov, J. *Phys. Rev. Lett.* **1998**, *81*, 2819–2822.

(47) Strasser, P.; Koh, S.; Anniyev, T.; Greeley, J.; More, K.; Yu, C.; Liu, Z.; Kaya, S.; Nordlund, D.; Ogasawara, H.; Toney, M. F.; Nilsson, A. *Nat. Chem.* **2010**, *2*, 454–

460.

(48)   Escudero-Escribano, M.; Malacrida, P.; Hansen, M. H.; Vej-Hansen, U. G.; Velazquez-Palenzuela, A.; Tripkovic, V.; Schiotz, J.; Rossmeisl, J.; Stephens, I. E. L.; Chorkendorff, I. *Science (80-.).* **2016**, *352*, 73–76.

(49)   Wang, H.; Xu, S.; Tsai, C.; Li, Y.; Liu, C.; Zhao, J.; Liu, Y.; Yuan, H.; Abild-pedersen, F.; Prinz, F. B.; Nørskov, J. K.; Cui, Y. *Science (80-.).* **2016**, *354*, 1031–1036.

(50)   Balko, E. N.; Davidson, C. R. *J. Inorg. Nucl. Chem.* **1980**, *42*, 1778–1781.

(51)   Wanjala, B. N.; Luo, J.; Loukrakpam, R.; Fang, B.; Mott, D.; Njoki, P. N.; Engelhard, M.; Naslund, H. R.; Wu, J. K.; Wang, L.; Malis, O.; Zhong, C. J. *Chem. Mater.* **2010**, *22*, 4282–4294.

(52)   Liao, H.; Fisher, A.; Xu, Z. J. *Small* **2015**, *11*, 3221–3246.

(53)   Tang, X.; Li, Y.; Huang, X.; Xu, Y.; Zhu, H.; Wang, J.; Shen, W. *Appl. Catal. B Environ.* **2006**, *62*, 265–273.

(54)   Di Cosimo, J. I.; Díez, V. K.; Xu, M.; Iglesia, E.; Apesteguía, C. R. *J. Catal.* **1998**, *178*, 499–510.

(55)   Schoeb, A. M.; Raeker, T. J.; Yang, L.; Wu, X.; King, T. S.; Depristo, A. E. **1992**, *278*, 2–7.

(56)   Christoffersen, E.; Liu, P.; Ruban, A.; Skriver, H. .; Nørskov, J. . *J. Catal.* **2001**, *199*, 123–131.

(57)   Novell-Leruth, G.; Carchini, G.; López, N. *J. Chem. Phys.* **2013**, *138*, 17886–17892.

(58)   Garcia-Mota, M.; Vojvodic, A.; Metiu, H.; Man, I. C.; Su, H. Y.; Rossmeisl, J.; Nørskov, J. K.; García-Mota, M.; Vojvodic, A.; Metiu, H.; Man, I. C.; Su, H. Y.; Rossmeisl, J.; Nørskov, J. K. *ChemCatChem* **2011**, *3*, 1607–1611.

(59)   Kim, H. Y.; Lee, H. M.; Pala, R. G. S.; Shapovalov, V.; Metiu, H. *J. Phys. Chem. C* **2008**, *112*, 12398–12408.

(60)   He, H.; Zapol, P.; Curtiss, L. a. *Energy Environ. Sci.* **2012**, *5*, 6196.

(61)   Karlsson, R. K. B.; Cornell, A.; Pettersson, L. G. M. *Electrochim. Acta* **2015**, *180*, 514–527.

(62)   Bhowmik, A.; Hansen, H. A.; Vegge, T. *J. Phys. Chem. C* **2017**, *121*, 18333–18343.

(63)   Kresse, G. *Phys. Rev. B* **1999**, *59*, 1758–1775.

(64)   Wellendorff, J.; Lundgaard, K. T.; Møgelhøj, A.; Petzold, V.; Landis, D. D.; Nørskov, J. K.; Bligaard, T.; Jacobsen, K. W. *Phys. Rev. B* **2012**, *85*, 235149.

(65)   Lee, K.; Murray, É. D.; Kong, L.; Lundqvist, B. I.; Langreth, D. C. *Phys. Rev. B -*

Condens. Matter Mater. Phys. **2010**, *82*, 3–6.

(66) Liu, W.; Carrasco, J.; Santra, B.; Michaelides, A.; Scheffler, M.; Tkatchenko, A. *Phys. Rev. B - Condens. Matter Mater. Phys.* **2012**, *86*, 1–6.

(67) Ramalho, J. P. P.; Gomes, J. R. B.; Illas, F. *RSC Adv.* **2013**, *3*, 13085.

(68) Nørskov, J. K.; Rossmeisl, J.; Logadottir, A.; Lindqvist, L.; Kitchin, J. R.; Bligaard, T.; Jónsson, H. *J. Phys. Chem. B* **2004**, *108*, 17886–17892.

(69) Zafeiratos, S.; Piccinin, S.; Teschner, D. *Catal. Sci. Technol.* **2012**, *2*, 1787.

(70) Hoffmannová, H.; Okube, M.; Petrykin, V.; Krtil, P.; Mueller, J. E.; Jacob, T. *Langmuir* **2013**, *29*, 9046–9050.

(71) Mayrhofer, K. J. J.; Juhart, V.; Hartl, K.; Hanzlik, M.; Arenz, M. *Angew. Chemie - Int. Ed.* **2009**, *48*, 3529–3531.

(72) Shi, C.; O'Grady, C. P.; Peterson, A. a; Hansen, H. a; Nørskov, J. K. *Phys. Chem. Chem. Phys.* **2013**, *15*, 7114–7122.

(73) Back, S.; Kim, J.H.; Kim, Y.T.; Jung, Y. *Phys. Chem. Chem. Phys.* **2016**, *18*, 9652–9657.

(74) Yoo, J. S.; Christensen, R.; Vegge, T.; Nørskov, J. K.; Studt, F. *ChemSusChem* **2016**, *9*, 358–363.

(75) Kuhl, K. P.; Hatsukade, T.; Cave, E. R.; Abram, D. N.; Kibsgaard, J.; Jaramillo, T. F. *J. Am. Chem. Soc.* **2014**, *136*, 14107–14113.

(76) Jovanov, Z. P.; Hansen, H. A.; Varela, A. S.; Malacrida, P.; Peterson, A. A.; Nørskov, J. K.; Stephens, I. E. L.; Chorkendorff, I. *J. Catal.* **2016**, *343*, 215–231.

(77) Abild-Pedersen, F.; Greeley, J.; Studt, F.; Rossmeisl, J.; Munter, T. R.; Moses, P. G.; Skulason, E.; Bligaard, T.; Nørskov, J. K. *Phys. Rev. Lett.* **2007**, *99*, 16105.

(78) Lee, Y.-L.; Kleis, J.; Rossmeisl, J.; Shao-Horn, Y.; Morgan, D. *Energy Environ. Sci.* **2011**, *4*, 3966.

(79) Han, B.; Risch, M.; Lee, Y.-L.; Ling, C.; Jia, H.; Shao-Horn, Y. *Phys. Chem. Chem. Phys.* **2015**, *17*, 22576–22580.

(80) Suntivich, J.; May, K. J.; Gasteiger, H. A.; Goodenough, J. B.; Shao-Horn, Y. *Science (80-.).* **2011**, *334*, 1383–1385.

(81) Calle-Vallejo, F.; Inoglu, N. G.; Su, H.-Y.; Martínez, J. I.; Man, I. C.; Koper, M. T. M.; Kitchin, J. R.; Rossmeisl, J. *Chem. Sci.* **2013**, *4*, 1245.

(82) Mattheiss, L. *Phys. Rev. B* **1976**, *13*, 2433–2450.

(83) Daniels, R. R.; Margaritondo, G.; Georg, C. A.; Lévy, F. *Phys. Rev. B* **1984**, *29*, 1813–1818.

(84) Tang, W.; Sanville, E.; Henkelman, G. *J. Phys. Condens. Matter* **2009**, *21*, 84204.

(85) Kim, Y. D.; Seitsonen, A. P.; Over, H. *Phys. Rev. B* **2001**, *63*, 115419.

(86) Sun, W.; Song, Y.; Gong, X.-Q.; Cao, L.; Yang, J. *Chem. Sci.* **2015**, *6*, 4993–4999.

(87) Stamenkovic, V.; Mun, B. S.; Mayrhofer, K. J. J.; Ross, P. N.; Markovic, N. M.; Rossmeisl, J.; Greeley, J.; Nørskov, J. K. *Angew. Chemie* **2006**, *118*, 2963–2967.